Check for updates

MATERIALS SCIENCE

Bioadaptive liquid-infused multifunctional fibers for long-term neural recording via BDNF stabilization and enhanced neural interaction

Tae Young Kim¹†, Yeonzu Son²†, Keun-Young Yook¹, Dong Gyu Lee³, Young Kim^{4,5,6}, Seo Jung Kim⁷, Kijun Park¹, Yurim Lee¹, Tae Kyung Lee^{3,8}, Justin J. Chung^{4,5,9}, Congqi Yang¹⁰, Seongjun Park^{10,11,12,13}*, Jungmok Seo¹*

Brain-computer interfaces (BCIs) enable direct communication between the brain and computers. However, their long-term functionality remains limited due to signal degradation caused by acute insertion trauma, chronic foreign body reaction (FBR), and biofouling at the device-tissue interface. To address these challenges, we introduce a multifunctional surface modification strategy called targeting-specific interaction and blocking nonspecific adhesion (TAB) coating for flexible fiber, achieving a synergistic integration of mechanical compliance and biochemical stability. The coating combines brain-derived neurotrophic factor (BDNF) conjugation and a lubricant-infused surface. This dual-functional design enables selective interaction with neurons and astrocytes while preventing nonspecific adhesion. Notably, high-quality single-unit neural signals were stably recorded for more than 12 months after implantation, demonstrating exceptional long-term recording performance. Integrating mechanical compatibility, antifouling properties, and selective neural cell interaction, the TAB-coated multifunctional fiber represents a transformative approach for neural implants, bridging biological systems with computational systems.

Copyright © 2025 The Authors, some rights reserved; exclusive licensee American Association for the Advancement of Science. No claim to original U.S.
Government Works.
Distributed under a Creative Commons Attribution
NonCommercial
License 4.0 (CC BY-NC).

INTRODUCTION

Brain computer interface (BCI) is a system that enables direct communication of computer with neural system (1–3). One notable example of BCI is an implantable neural device that is directly inserted into brain allowing interaction between the central nervous system (CNS) and computer (4). This innovation has received substantial attention due to its potential application in various fields ranging from medical therapies to cognitive enhancement (5–11). For these applications, the neural devices should be seamlessly integrated with the human brain and stably operated for the long term (12–15). Moreover, the implantable neural devices require high resolution and fidelity in data acquisition to allow precise interaction with the nervous system. However, conventional implantable neural devices have limitations such as nonselective adhesion of cells, foreign body reaction (FBR), glial sheath formation around the implanted site (16–18), and continuous damages inflicted by micromotion (19).

¹School of Electrical and Electronic Engineering, Yonsei University, 50-1 Yonsei-ro, Seodaemun-gu, Seoul 03722, Republic of Korea. ²Program of Brain and Cognitive Engineering, Korea Advanced Institute of Science and Technology, Daejeon 34141, Republic of Korea. ³Department of Materials Engineering and Convergence Technology, Gyeongsang National University, 501 Jinju-daero, Jinju 52828, Republic of Korea. ⁴Department of Transdisciplinary Medicine, Seoul National University Hospital, Seoul 03080, Republic of Korea. ⁵Innovative Medical Technology Research Institute, Seoul National University Hospital, Seoul 03080, Republic of Korea. ⁶Department of Clinical Medical Sciences, Seoul National University College of Medicine, Seoul 03080. Republic of Korea. ⁷Department of Pediatrics, Severance Children's Hospital, Yonsei University College of Medicine, Seoul 03722, Republic of Korea. 8School of Materials Science and Engineering, Gyeongsang National University (GNU), 501 Jinju-daero, Jinju 52828, Republic of Korea. ⁹Department of Medicine, Seoul National University College of Medicine, Seoul 03080, Republic of Korea. ¹⁰Medical Research Center, Seoul National University, Seoul 03080, Republic of Korea. ¹¹Department of Biomedical Sciences, College of Medicine, Seoul National University, Seoul 03080, Republic of Korea. ¹²School of Transdisciplinary Innovations, Seoul National University, Seoul 08826, Republic of Korea. ¹³Interdisciplinary Program in Bioengineering, College of Engineering, Seoul National University, Seoul 08826, Republic of Korea.

*Corresponding author. Email: jungmok.seo@yonsei.ac.kr (J.S.); seongjunpark@snu.ac.kr (S.P.)

†These authors contributed equally to this work.

These issues notably shorten the life span of the neural device and decrease resolution and accuracy of neural signal recording. To ensure precise and long-term operation of the neural device, they should promote selective interaction with neuronal cells for reliable performance while minimizing the inflammation caused upon the implantation (20).

During the implantation, neural devices inevitably inflict acute inflammation, which can progress to chronic inflammation. One of the primary concerns is the acute trauma inflicted on the surrounding neural tissue during the surgical insertion process (21, 22). This initial damage can trigger a cascade of biological responses, including acute and chronic FBRs (17, 23-25). This often leads to glial scarring and eventual encapsulation of the device, which compromises signal quality and long-term functionality (26). The initiation of the immune cascade around implantable devices often begins with the adhesion of biomolecules and immune cells to the device surface (27). Surface modification has been investigated as a strategy to mitigate immune response (28). These biochemical strategies aim to prevent the adhesion of unwanted cells and proteins near the device surface, using various antifouling surface modification techniques such as hydrophilic, hydrophobic, and drug-loaded coatings (29). These surface modifications have demonstrated pronounced success in reducing biofouling and mitigating immune responses at the implantation site. However, while these coatings effectively repel unwanted substances, it is noteworthy that the strategies may not be an ideal interface for neural device implants requiring high-sensitivity signal recording as they inhibit direct interaction between the device and neurons (30). These limitations arise from the extreme repellency even against the target neurons. The potential hindrance of adhesion between neurons, glial cells, and the devices may lead to diminished neural recording sensitivity and selectivity.

Neural integrity remains a challenge to acquire neural signals with high resolution and fidelity. To establish a closer interface between the device and target neurons, recent strategies have explored the conjugation of biomolecules that promote selective interaction and support cell survival (31-33). However, the implanted biomolecule conjugates were reported to be subject to biodegradation as it is continuously exposed to proteolytic enzymes and immune responses. Proteases degrade proteins and peptides, while immune cells, such as macrophages and neutrophils, generate reactive oxygen species and other enzymes that further break down biomolecular coatings (34). These biochemical and cellular defense mechanisms recognize foreign materials and lead to the gradual degradation of biomolecules. In addition, biomolecule-coated implants do not adequately address the tissue trauma caused by friction of device insertion (35). These combined effects gradually compromise the implant's functionality and long-term stability. To overcome these limitations, it is essential to develop implantable devices that integrate neural cell affinity, antifouling properties, and flexibility into a unified design, ensuring both biochemical compatibility and mechanical harmony with the surrounding tissue.

To this end, we introduced a TAB (targeting-specific interaction and blocking nonspecific adhesion) coating for flexible neural fibers, incorporating brain-derived neurotrophic factor (BDNF) conjugation and a lubricated surface through partial silanization, aiming to achieve seamless mechanical and biochemical integration between the device and neural tissue. The coating consists of alternately immobilized perfluorosilane (PFS) and aminosilane to promote the selective interaction of neurons and astrocytes while preventing nonspecific adhesions of immune-related substances (36). The PFS component imparts low surface energy for holding a slippery lubricant layer, while the aminosilane serves as an anchor for BDNF. The immobilized BDNF facilitates the interaction of neurons and astrocytes with the device by binding to tropomyosin receptor kinase B (TrkB) receptors (28, 37-39). The thin lubricant layer repels nonspecific adhesions reducing the attachment of blood and plasma proteins to less than 3%. The antifouling properties against plasma protein were confirmed, and selective interactions with brain cells were tested under in vitro conditions. Notably, it exhibited increased adhesion of astrocytes and neurons, reaching ~25% coverage after 1 day and proliferating up to 65% after 1 week. These findings highlight the dual functionality of the TAB coating in suppressing adhesion of immune cells while promoting selective interaction with neuronal cells. Furthermore, TAB coating-applied flexible neural fiber was implanted in vivo in mouse models, showing long-term signal recording (>1 year) with a higher signal recording sensitivity compared to pristine neural fiber. Histological analysis and biomechanical tests confirmed enhanced target cell interaction selectivity and prolonged implant periods. This bioactivated lubricated surface presents a promising dual-action strategy for implantable neuronal devices, improving integration with brain tissue.

RESULTS

Design and principle of the multifunctional fibers with TAB coating

We fabricated neural probes based on flexible fibers with TAB coating, designed to enhance biochemical mitigation alongside mechanical mitigation (Fig. 1A). First, to achieve mechanical mitigation, flexible multifunctional neural fiber was fabricated through a thermal drawing process (TDP). This process allows miniaturization and integration of functional modalities into fibers by preserving the cross-sectional structure. This microscale polymeric fiber

exhibits exceptional flexibility, demonstrated by its flexural rigidity of 1.49×10^{-7} N/m². Moreover, a single fiber device is capable of primary functions required for neural interfaces, including electrophysiologic (e-phys) recording of single neuron spiking activities, optogenetic stimulation, and microfluidic drug delivery. Subsequently, TAB coating was applied to enhance the neural interaction and longevity of the signal record. The TAB coating is based on PFS layer with partially immobilized BDNF molecules within its structure. Upon lubricant infusion on the PFS, the coating exhibits frictionless properties, minimizing friction during insertion and reducing adverse acute insertion trauma. In addition, it demonstrates antifouling against coagulation agents (e.g., thrombin and fibrinogen), preventing the initiation of FBR and inflammatory reactions. The partially immobilized BDNF within the PFS layer promotes interactions with neurons and astrocytes, supporting the survival and growth of the neurons and astrocytes. BDNF is closely linked to the promotion of the A2 astrocyte subtype which is considered neuroprotective because it up-regulates the expression of neurotrophic factors (40, 41), which support neuronal survival (42), regeneration (41), and repair (43). In addition, BDNF is known to increase the metabolic functions of astrocytes converting glucose into lactate via glycolysis (44, 45), and the lactate can then be shuttled to neurons as an energy source. Despite its numerous advantages, BDNF is known to degrade rapidly in vivo conditions due to the resident immune system and proteolytic enzymes. Recent studies have shown that intracerebral injection of BDNF can trigger a localized inflammatory response from resident immune cells such as microglia. Once activated, these immune cells not only degrade foreign biomolecules directly, causing BDNF levels to decrease notably within 2 hours postinjection, but also release proteolytic enzymes. In addition, this immune activation may initiate the early stages of the FBR, leading to glial sheath formation around implanted neural fibers later. This phenomenon hinders interaction between the implant surface, neurons, and astrocytes interrupting the bioactivity of target cells (Fig. 1B). However, the TAB coating's thin lubricant layer prevents immune cell adhesion and migration to the BDNF which prevents immune cell activation. Moreover, TAB coating demonstrates bioactivity by inducing the spreading and proliferation of adhered astrocytes, along with increased gene and protein levels of antioxidant and glycolysis, promoting successful neural integration (Fig. 1C). These synergic effects of physical compatibility, biocompatibility (neuronal integrity), and antifouling capability enable the realization of high resolution and longevity of signal recording (Fig. 1D). We confirm the long-term recording of neural signals with a mouse in vivo model over a year, whereas the uncoated group loses signal recording a few months later (Fig. 1E).

Fabrication process of multifunctional fibers and TAB coatings and characterization

TDP allows the centimeter-to-micrometer level scale-down of cross sections of the thermoplastic polymer preform based on polycarbonate (PC) and polymethyl methacrylate (PMMA) (Fig. 2A). The preform includes three channels, two for threading tungsten microwires and the other to form a hollow channel. In TDP, the polymer preform is heated beyond its glass transition temperature to undergo elongation, whereby the cross section gradually diminishes to form fibers. Throughout the process, the size of the channels proportionally diminishes, converging to match the diameter of the metal wire. Hence, the PC/PMMA fiber is codrawn with tungsten

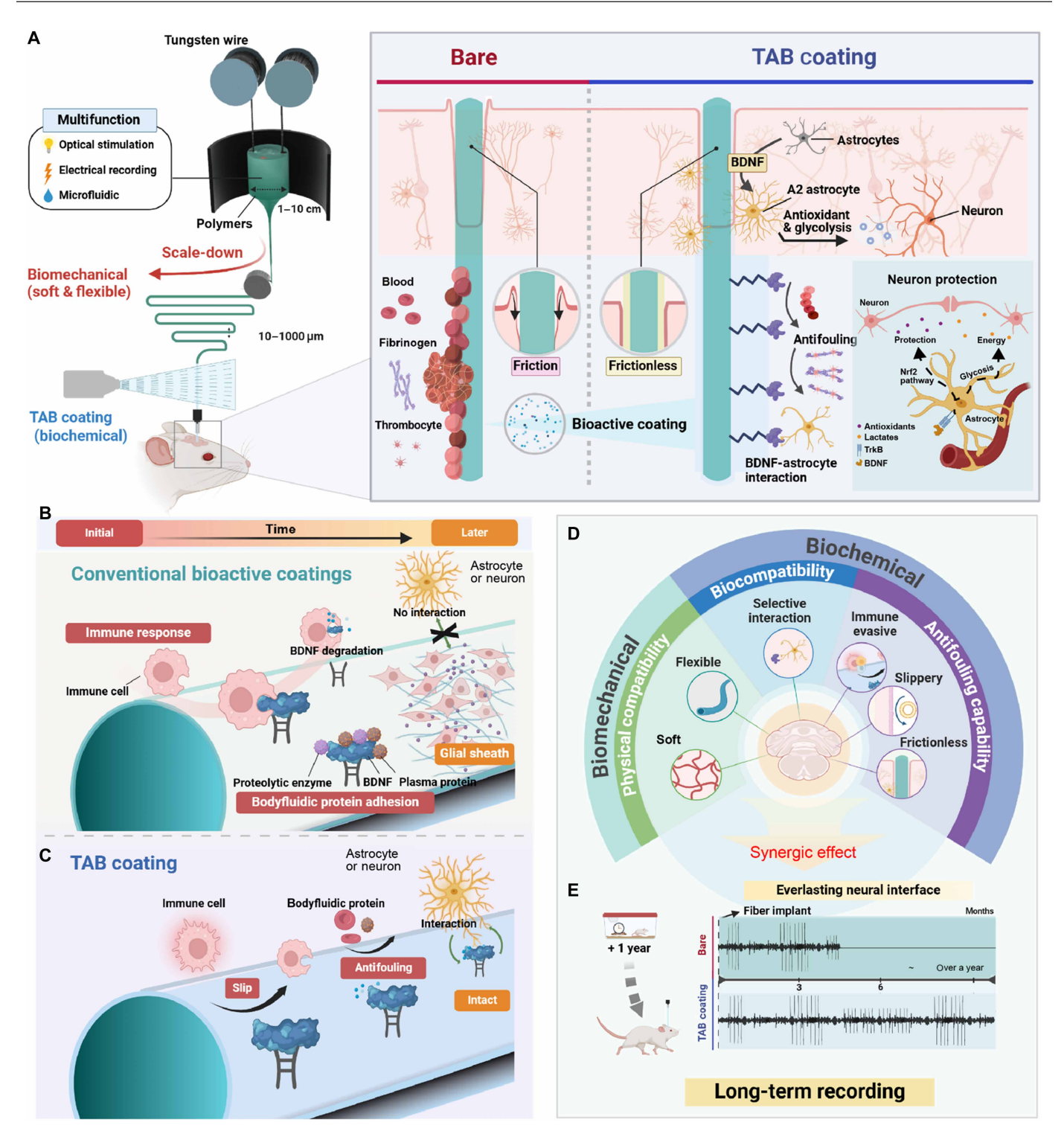


Fig. 1. Design and principle of the multifunctional neural fiber with TAB coating. (A) The fabrication schematic illustration of neural fiber using TDP and characteristics of TAB coating. (B and C) Schematics of conventional bioactive and TAB coating in in vivo conditions. (D and E) Summary diagram of experimentally validated synergistic effects of flexible neural fibers and TAB coating, illustrating mechanical and biochemical advantages.

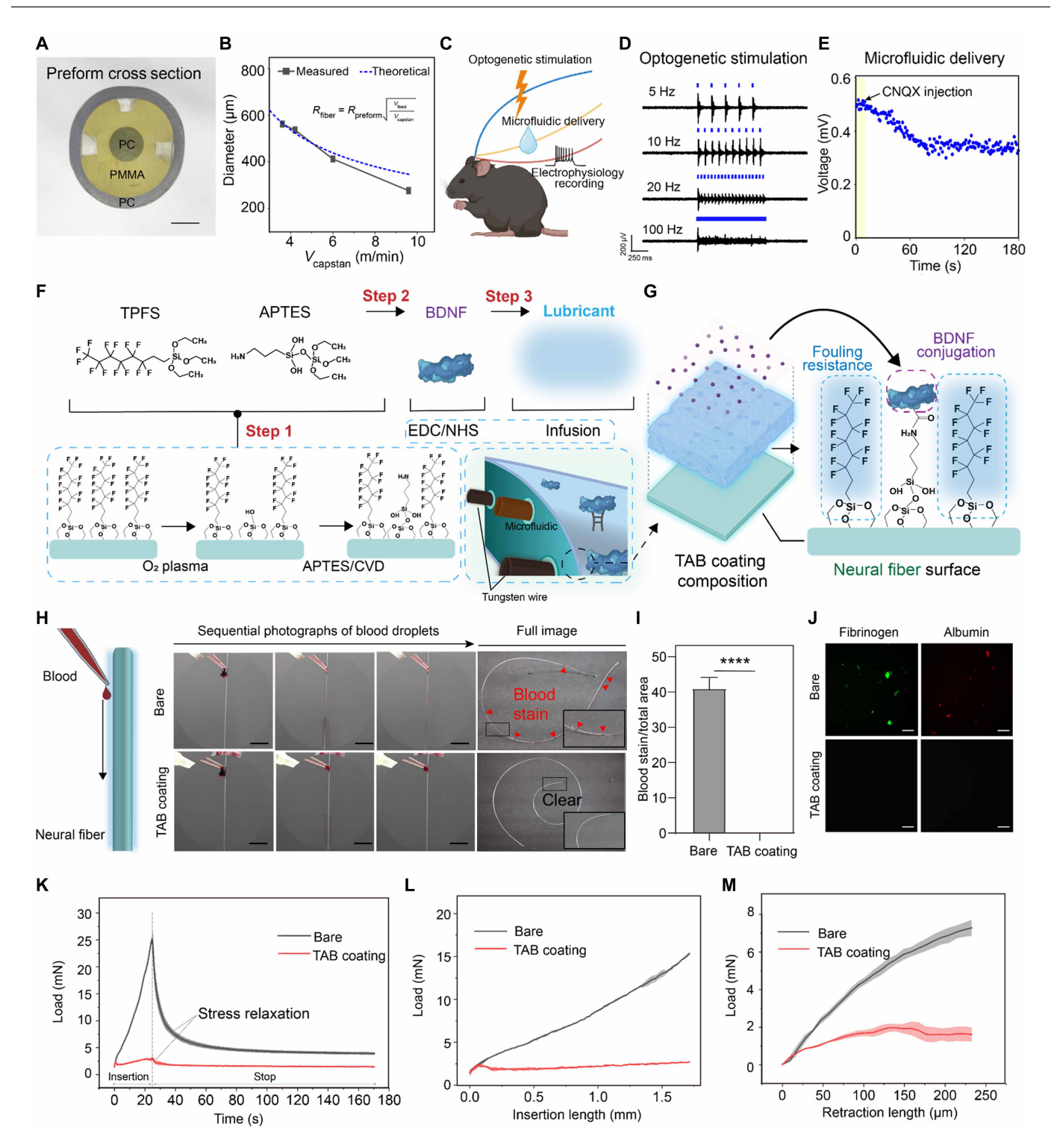


Fig. 2. Fabrication process of fibers and TAB coating and characterization. (**A**) Photograph of the fiber cross section. Scale bar, 5 mm. (**B**) Multifunctional fiber fabrication according to the capstan speed during the TDP. (**C**) Schematic illustration of the multifunctionality of the fiber. (**D**) Optically evoked potential recorded in response to optogenetic stimulation at 5, 10, 20, and 100 Hz. Blue dots indicate the delivery of optical stimulation pulses. (**E**) Microfluidic delivery of synaptic blocker (CNQX) blocking optogenetic stimulation. (**F** and **G**) Schematics illustrate the stepwise fabrication process of TAB coating and its composition. CVD, chemical vapor deposition. (**H** to **J**) Evaluation of antifouling properties of TAB coating against blood droplets and plasma proteins (fibrinogen and albumin) (n = 4). Scale bars, 0.5 cm and 100 μ m. (**K** and **L**) Load exerted during and after the insertion of bare and TAB fiber into the phantom brain (n = 3). (**M**) Load exerted during the retraction of bare and TAB fiber from the phantom brain (n = 3) (*****P < 0.0001).

wires, which forms a 276 \pm 1.52 μ m-diameter multifunctional fiber including the optical waveguide, microfluidic channel, and microelectrode (Fig. 2B and fig. S1). The multifunctionality of our device allows targeted on-site neuromodulation, which can be monitored simultaneously. The fiber is evaluated to have an optical transmission loss of -1.14 dB/cm (fig. S2), which makes it suitable for optogenetic stimulation. The optical and electrical functionalities have been implemented and tested in different frequencies of optical pulses (Fig. 2C). The fiber device successfully transmitted blue light to the transgenic Thy1-ChR2-eYFP mouse brain, where the optical pulses evoked electrical potential in ChR2-expressing neurons, which were recorded simultaneously (Fig. 2D). The peak-to-valley amplitudes of optically evoked potential are consistent throughout the trial in response to low-frequency pulses (5 and 10 Hz). In contrast, they markedly decrease in response to high-frequency pulses (20 and 100 Hz), demonstrating excitation behavior of neurons with no sign of optical artifact. Furthermore, the fiber facilitates local inhibition of neural activity through direct injection of synaptic blocker [cyanquixaline (6-cyano-7-nitroquinoxaline-2,3-dione (CNQX)] through microfluidic channel (Fig. 2E and fig. S3). Delivery of CNQX during optical stimulation blocks the excitatory synaptic activities at the site, as evidenced by the diminished excitatory responses to 1-Hz optical pulses.

By rendering the surface chemistry of the multifunctional fiber to match that of the lubricant, the substrate is able to hold a lubricant layer. To incorporate BDNF anchoring, we designed a fluorine-terminated substrate surface that also includes amine groups. This was accomplished through a partial silanization method, selectively replacing some fluorine-terminated groups with aminosilanes. Figure 2 (F and G) shows the detailed fabrication process of TAB coating, which involves three major steps. First, the substrate is initially treated with oxygen plasma to form an oxygen group on the surface. The oxidized surface then reacts with the silane group of fluorosilane polymer (PFS), forming a covalent bond. Next, a second oxygen plasma treatment is applied to the fluorosilanized substrate to remove some of the fluorine group. The exposed regions are then treated with 3-aminopropyltriethoxysilane (APTES) using a chemical vapor deposition method. We confirmed partial alternation of PFS to APTES by x-ray photoelectron spectroscopy (XPS). In the second step, BDNF was covalently immobilized onto the APTES through carbodiimide chemistry using 1-ethyl-3-(3 dimethylaminopropyl)carbodiimide (EDC) and N-hydroxysuccinimide (NHS). The TAB coating is lastly completed by infusing a perfluoropolyether (PFPE) lubricant onto the substrate. The thin lubricant layer prevents the nonspecific adhesion of biomolecules and immune cells while allowing the immobilized BDNF to simultaneously promote target cell adhesion of the neurons. Changes in the chemical characteristics due to surface modification were confirmed with XPS (fig. S4A). We optimized the partial silanization process by adjusting the ratio between fluorosaline and APTES which can be tuned by varying the duration and intensity of the secondary O₂ plasma treatment. First, we fixed the O₂ plasma power intensity at 30 W followed by the previous report. Our goal was to create a fluorinated hydrophobic surface with APTES distributed uniformly. We confirmed that the amount of PFS molecules on the surface could be regulated by adjusting the secondary O₂ plasma time. Loss of hydrophobicity was observed after 10 s of secondary

O₂ plasma, resulting in contact angle (CA) decreasing to below 90° (fig. S4B). Therefore, we concluded that treating the surface with O₂ plasma at 30 W power for 5 s was optimal to ensure sufficient fluorination for lubricant retention and adequate amine deposition of BDNF immobilization. The TAB coating was applied to the neural fiber surface, and then antifouling capabilities against various solvents were used in biomedical applications, which are distilled (DI) water, fetal bovine serum, blood, ethylene glycol, and dimethyl sulfoxide (DMSO) (fig. S4C). We conducted ultraviolet-visible spectroscopic measurements to assess the optical transparency of the TAB-coated glass. The results indicated a slight reduction in transmittance following the TAB coating process. Despite this minor decrease, the optical properties remained within acceptable ranges, demonstrating that the coating did not notably hinder the optogenetic functionality of the multifunctional fiber (fig. S4D). This observation confirms the compatibility of the TAB coating with optogenetic applications, ensuring effective light transmission without compromising performance. The TAB-coated surface demonstrated hydrophobicity regardless of the solvent's surface tension. In addition, the TAB-applied neural fiber demonstrates antifouling properties against horse blood and plasma proteins (fibrinogen and albumin). We observed that bare neural fiber was stained by blood when the blood dropped alongside the fiber with sequential optical photographs (Fig. 2, H and I, and movie S1). However, TAB-applied neural fiber showed a clear stain-free surface. Fluorescence images further confirmed the absolute antifouling capability of TAB-applied fibers against plasma proteins, while bare neural fiber showed adhesion of the plasma proteins (Fig. 2J and fig. S3, E and F). Furthermore, TAB coating endows the device with the frictionless properties. The coating has markedly decreased the load applied to the phantom brain (0.6% agarose gel) during and after insertion (Fig. 2, K and L). The TAB coating's lubricant allows the coated fiber to slip during insertion, and the insertion load transiently decreases after slipping. The insertion load has increased almost linearly with the bare fiber upon insertion. Conversely, the lubrication on the fiber allows a marked decrease in the maximum insertion load from 25.2 to 2.94 mN. Moreover, the frictionless behavior of our device leads to distinct stress relaxation behaviors, resulting in a lower load of 1.45 mN after the saturation compared to a bare device (3.94 mN). The results suggest that the slipping behavior allowed by lubricant coating can notably reduce the mechanical stress applied to the brain during and after the fiber insertion process. Moreover, the coated fiber exerts a less frictional load on the implant site than the bare fiber during retraction (Fig. 2N). Hence, less mechanical damage in response to the chronic micromotion is expected at our device-tissue interface during the long-term implantation. To further evaluate the long-term stability of the TAB coating under physiologically relevant conditions, we performed a standardized cross-cut adhesion test (ASTM D3359) using a tape-peeling method (fig. S5). The TAB coating surface maintained structural integrity even after 10 repetitive tape-peeling cycles, indicating strong adhesion and mechanical stability. In contrast, a conventional poly(ethylene glycol)-based antifouling coating showed complete delamination after only 5 cycles. These results highlight the superior mechanical durability of the TAB coating compared to existing antifouling materials, which is essential for chronic in vivo neural implantation.

In vitro evaluation of immune response and interaction with target cells

To gain molecular-level insight into the behavior of lubricant molecules on trichloro(1H,1H,2H,2H-perfluorooctyl)silane TPFS/ APTES-coated surface, molecular dynamics (MD) simulations were performed (Fig. 3A). The analysis of the concentration profile of lubricant molecules on the surface of TPFS/APTES revealed that the lubricant molecules interacted more extensively with TPFS regions than APTES regions (Fig. 3B and fig. S6). Quantitatively, the integrated areas of concentration profile for the lubricant molecules were 114.53 Å in the TPFS region and 15.09 Å in the APTES region, indicating a 7.6-fold higher localization in the TPFS region (Fig. 3C). The relatively low interaction between APTES and lubricant demonstrates that lubricant molecules tend to detach or redistribute from an APTES-coated region. This preferential localization on PFS leads to exposure of BDNF on the implant surface. Consequently, the surface develops a lubricant island pattern, where highly lubricated PFS regions are interspersed with BDNF-exposed APTES domains. This heterogeneous surface distribution offers spatial control over cellular interactions. The exposed BDNF enhances adhesion and communication with neurons and astrocytes, facilitating their interaction with the implant interface. In contrast, the lubricant-rich PFS regions lead to unstable adhesion and activation of immune cells such as microglia and macrophages. This selective repellence mechanism ensures that immune cells fail to anchor stably, reducing local immune activation and inflammation. To systematically verify this phenomenon, MD simulation was further conducted on the 1:1 ratio of TPFS/APTES configuration (fig. S7). The 1:1 ratio also revealed a comparable trend, where TPFS regions were more involved in interactions with the lubricant, as observed in the 8:2 ratio case. As a complementary analysis, density functional theory calculations were performed to examine the electrostatic potential isosurface of the molecules (fig. S8A). The TPFS molecule exhibited a broader and more evenly distributed negative electrostatic potential, especially on its exposed surface, compared to APTES molecule. On the other hand, the lubricant molecule exhibited relatively positive regions, suggesting a favorable electrostatic interaction with TPFS. Moreover, it was further supported by the calculations of binding energies, which showed a stronger interaction between the lubricant and TPFS than with APTES (fig. S8B). To improve therapeutic efficacy, medical implants often need to have bioactivity that influences cellular behaviors including cell migrations (fig. S9) and interaction with surrounding tissues. However, biomolecule-immobilized surfaces are affected by degradation in a few minutes or hours by resident immune cells and proteolytic enzymes. When the device was implanted with only the immobilized BDNF but no lubricant layer, the BDNF on the implant's surface would be exposed directly to the body's immune system (Fig. 3D). Immune cells, such as microglia in the CNS, recognize these biomolecules as foreign materials. The recognition could trigger an immune response aimed at eliminating or neutralizing the foreign materials. The immune response might result in the degradation of the biomolecules on the implant's surface, effectively breaking them down and rendering them inactive. In addition, the immune cells could release proinflammatory cytokines, signaling molecules that promote inflammation. These phenomena could further disrupt the device's function by damaging nearby tissue or altering the environment around the implant, hindering its ability to record neuronal signals accurately. However, the outcome would be notably different in the case of the device applied with the

TAB coating. The coating offers an optimal environment for longterm and precise neuronal signal recording by reducing immune system interference in both short- and long-term and promoting selective interaction with neurons and astrocytes. The immobilized BDNF is designed to enhance specific cellular interactions that are beneficial for neuronal survival. Meanwhile, the lubricant layer acts as a protective barrier, preventing unwanted immune system interactions by minimizing adhesion to the device's surface. The lubricant layer is crucial in ensuring that the biomolecules remain active and long-term neural signal recording without triggering an immune response. We expected that a TAB-coated surface would interact with brain tissues which induces an antioxidant pathway through the Nrf2 signal cascade. In addition, interaction between BDNF and astrocyte up-regulates glycolysis resulting in lactate production. The lactate usually is used as an energy source of neurons which helps neurons survive. In Fig. 3E, we confirmed selective cell adhesion with primary hippocampal cells, including a mix of different cell types, primarily neurons along with glial cells. We conducted immunofluorescence staining to confirm cell adhesion selectivity. To investigate the cellular responses to each surface condition, we seeded primary hippocampal cell mixtures on bare, lubricant-, BDNF-, and TAB-coated dishes and evaluated the relative abundance of astrocytes, neurons, and microglia after 3 days. The astrocyte (green) and neuron (red) demonstrated a well-adhered and spreading TAB-coated surface, while microglia (purple) slightly adhered to it, showing a round shape, which demonstrates microglia remain in nonstimulated conditions. However, BDNF-immobilized surface without lubricant demonstrated not only neuron and astrocyte well-adhered but also microglia undergoing morphological transition, from rounded to ramified, meaning that microglia were also activated. Quantitative fluorescence analysis revealed that both BDNF- and TAB-coated groups exhibited notably higher astrocyte and neuron signal intensities, suggesting enhanced neural cell adhesion on neurotrophic surfaces (fig. S10, A and B). In contrast, microglial signal intensity was markedly reduced in the TAB-coated group relative to bare and BDNF groups (fig. S10C), indicating suppressed immune activation. In addition, morphological quantification of microglia further confirmed this observation; TAB-coated surfaces induced a rounded, nonactivated phenotype, whereas bare and BDNF groups exhibited a ramified activated morphology with a higher aspect ratio (fig. S10D). These results suggest that TAB coating promotes selective neural cell interaction while attenuating microglial activation. Matrix metalloproteinase 9 (MMP-9) concentrations of bare, lubricant-coated, BDNF-coated, and TAB-coated surfaces were determined in parallel using the enzyme-linked immunosorbent assay (ELISA) test (Fig. 3F). The cell culture media concentration of MMP-9 was notably higher in BDNF-coated without the lubricant group. The increasing levels of MMP-9 are involved in the degradation of extracellular matrix components and can also break down proteins like BDNF. When BDNF, or any foreign protein, is introduced into the body, it can be recognized by the immune system. If the immune cells, like microglia in the CNS, identify BDNF as a foreign or nonself-protein, then they may respond by degrading it. The release of proinflammatory cytokines such as tumor necrosis factor- α (TNF- α), interleukin-6 (IL-6), and IL-8 often accompanies the process of recognizing foreign proteins by immune cells. In the context of BDNF degradation, this inflammatory response would likely be mild, as BDNF is a small protein and not typically highly immunogenic. In Fig. 3 (G to I), the ELISA results demonstrate that

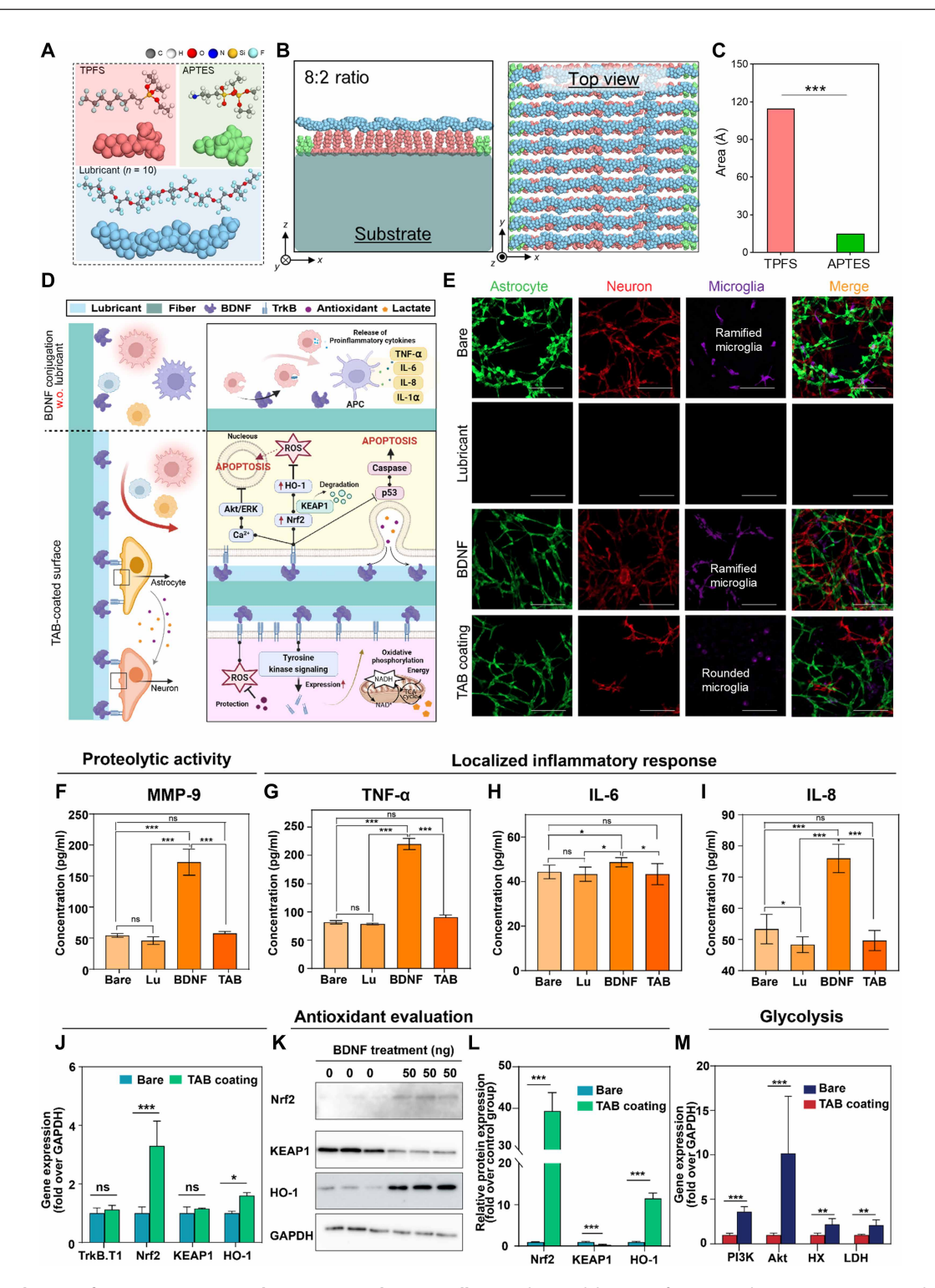


Fig. 3. In vitro evaluation of immune response and interaction with target cells. (A and B) Model systems for MD simulations. For an 8:2 ratio, the number of PFS, APTES, and lubricant (n = 10) molecules are 160, 40, and 40, respectively. (C) Quantitative analysis of the lateral area occupied by individual TPFS and APTES molecules on the surface, based on the top-view configuration. (D) Schematics of interactions between various cells and BDNF-conjugated coating and TAB coating. NADH, reduced form of NAD+; TCA, tricarboxylic acid; NAD+, nicotinamide adenine dinucleotide (oxidized form). (E) Representative fluorescence images for evaluation of neuron cells' interaction with the coated surface using immunofluorescence analysis (green, astrocyte; red, neuron; purple, microglia) (n = 4). Scale bars, 100 μ m. (F to I) Confirmation of proteolytic activity and localized inflammatory response against various conditions (bare, lubricant coated, BDNF conjugated, and TAB coating) (n = 3). (J to L) Evaluation of up-regulation of antioxidant pathways with qPCR and Western blot (n = 7). (M) Evaluation of up-regulation of glycolysis with qPCR (n = 7). (*P < 0.05, **P < 0.01, ***P < 0.001). ns, not significant.

TNF-α, IL-6, and IL-8 concentrations are notably high in groups with BDNF coating but no lubricant. This mild immune response occurred in the BDNF-coated group with the absence of lubricant, while other groups showed no immune response, especially the TAB-coated group due to its lubricant antifouling properties. Figure 3 (J to L) demonstrates the gene and protein expression levels related to the tissue's antioxidant defense, as shown by quantitative polymerase chain reaction (qPCR) and Western blot analyses. TrkB is a receptor tyrosine kinase that BDNF primarily activates. Upon binding BDNF, TrkB undergoes dimerization and autophosphorylation, initiating several downstream signaling pathways critical for neuronal survival and protection against stress. TrkB activation by BDNF leads to downstream signaling that supports the Nrf2 pathway promoting antioxidant defenses and reducing oxidative stress in neurons. The combined activation of Nrf2 and TrkB pathways may provide a robust protective effect in neurodegenerative conditions, where oxidative stress and impaired neurotrophic support are common. In addition, to investigate the molecular mechanisms by which BDNF immobilization protects neuronal survival, we performed qPCR analysis of representative genes involved in prosurvival and proapoptotic pathways. As shown in fig. S11A, neurons cultured on BDNF-immobilized surfaces exhibited notably increased expression of Akt1, ERK2, and Bcl2, alongside reduced expression of the proapoptotic marker Bad, suggesting the activation of a cell survival signaling cascade. Now, we observed a notable down-regulation of canonical apoptotic markers, including p53, caspase-3, caspase-9, and Bax (fig. S11B), indicating effective suppression of apoptosis. These results support the hypothesis that BDNF conjugation on the fiber surface facilitates neuronal protection through coordinated modulation of survival and apoptotic signaling. Furthermore, BDNF in the CNS not only supports neuronal survival but also plays a role in regulating energy metabolism, particularly glycolysis. BDNF can enhance glycolysis by up-regulating the expression of glycolytic enzymes and glucose transporters, thereby increasing glucose uptake and utilization in neurons. Neurons have high energy demands, particularly in the CNS, where they must maintain ion gradients, synthesize neurotransmitters, and support synaptic activity. By promoting glycolysis, BDNF helps ensure that neurons have sufficient energy to meet their functional demands, especially under conditions of stress like surgery. This metabolic support is essential for neuroprotection, as it helps maintain adenosine triphosphate (APT) levels and prevents cellular damage due to energy deficits. As shown in Fig. 3N, we confirmed increased gene expression levels associated with glycolysis such as PI3K, Akt, HX, and LDH in the TAB-coated group. The fluorescence images, ELISA, qPCR, and Western data demonstrate reduced immune response meanwhile increased antioxidant and glycolysis due to its interaction with TAB coating.

In vivo evaluation of immune response and interaction with target cells in the short term

Bare implant materials without TAB coating would lead to undesirable biological reactions in vivo conditions. The implant surface is usually recognized as a foreign material, leading to plasma protein adhesion, activation of coagulation, and immune response (red box). However, TAB coating demonstrates antifouling capability against proteins and immune cells (green box) and elicits neurotrophic changes (blue box) at the device-tissue interface (Fig. 4A). To evaluate FBR response to the TAB-coated neural fiber before brain implantation, we conducted a subcutaneous implantation

study in mice. In this model, fibers with or without TAB coating were inserted under the dorsal skin, and histological analysis was performed 1 week postimplantation (fig. S12A). Hematoxylin and eosin (H&E) staining revealed dense immune cell infiltration around bare fibers, whereas notably fewer immune cells were observed near TAB-coated implants. Moreover, Masson's trichrome staining showed increased collagen accumulation around bare implants, indicating a fibrotic encapsulation process consistent with FBR (fig. S12B). In contrast, the TAB-coated group exhibited substantially lower collagen deposition and immune infiltration, confirming that the TAB coating mitigates FBR and promotes improved biocompatibility at the implant-tissue interface (fig. S12C). In response to fiber implantation, the brain initiates an immune response, which includes neuroinflammation characterized by various types of glial activation, aimed at segregating the implant from the nervous system. Immunohistochemistry (IHC) results suggest the TAB coating has minimized the expression of proteolytic enzyme and activated microglia at the device-tissue interface at 1 day and 1 week implantation, respectively, whereas only the BDNF-coated group has elevated their expression (Fig. 4B). The elevated expression of MMP-9 on day 1 postimplantation around the BDNF-coated group indicates that the absence of lubrication induces an enhanced enzymatic immune response (Fig. 4C). The increased proteolytic activity suggests that the coated BDNF is subjected to enzymatic degradation before triggering neurotrophic activities. In contrast, the TAB coating effectively shields the fiber from proteolytic immune response while also reducing frictional tissue damage and preventing protein adsorption. Nontriggered proteolytic activity results in a reduced expression of Iba1, the activated microglial marker, around TAB-coated fibers at week 1 postimplantation (Fig. 4D). The reduced expression of activated microglia suggests the reduced formation of scar tissue, enabling the direct interaction of the device with the neurons. On the other hand, elevated proteolytic activity around BDNF-coated fibers results in a higher expression of activated microglia and exacerbated formation of scar tissue (Fig. 4D). In Fig. 4E, IHC results from day 1 and week 1 postimplantation suggest the TAB-coated group has induced the transition of astrocytes into the neurotrophic A2 subtype. The expression of A2-specific protein S100A10 is notably higher at the TAB interface than the bare at both 1 day and 1 week postimplantation, suggesting a higher proliferation of neuron-protective astrocytes in the vicinity. (Fig. 4, F and G). Meanwhile, the neurotoxic reactive A1-specific protein, C3, is not elevated at the TAB interfaces at 1 day and 1 week postimplantation (Fig. 4, H and I, and fig. S13). The results are consistent at both day 1 and week 1 postimplantation, while astrocyte activation progressively increases over time in both groups (fig. S14A). This implies that the TAB coating induces astrocytic transition specifically directed to neuroprotective subtypes. The results suggest that the TAB group elicits neurotrophic changes at the interface, where coated BDNF remains intact until interacting with neighboring astrocytes, leading to an elevation of the expression of A2 subtypes.

In vivo evaluation of neuronal survival at the device-tissue interface

Subsequently, an in vivo evaluation of the neuron-friendly effect of TAB-coated fibers was performed (Fig. 5A). The neuronal population surrounding the fibers was altered in response to changes in glial expression following implantation. We analyzed the expression of neuronal marker, NeuN, along with Iba1 at various time points of

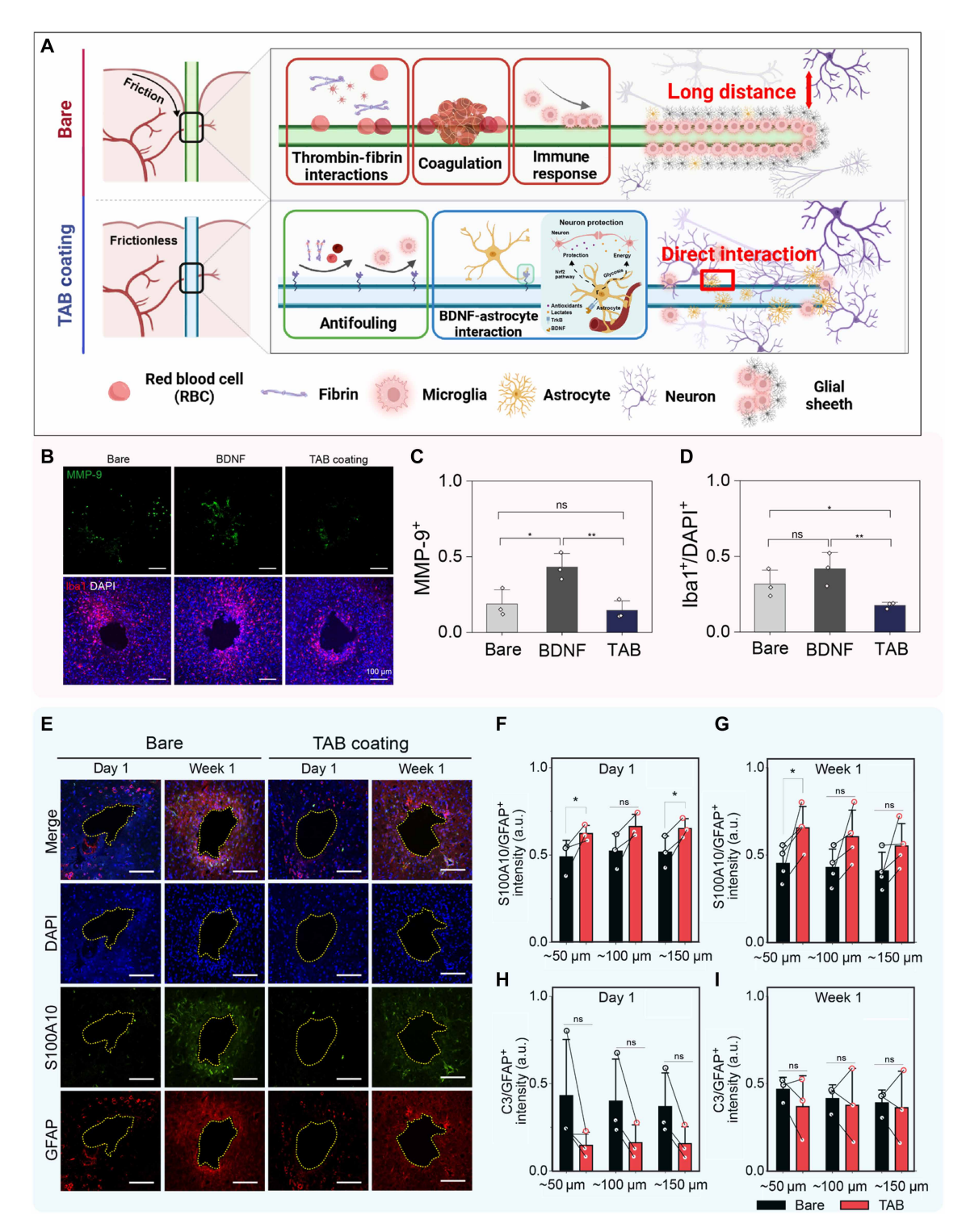


Fig. 4. In vivo evaluation of immune response and interaction with target cells in the short term. (**A**) Schematic illustration of the device-tissue interaction at the bare and TAB interfaces. (**B**) Representative confocal images of MMP-9 and Iba1 expression surrounding the fiber. Quantification of (**C**) proteolytic activity by MMP-9⁺ area and (**D**) activated microglial expression by Iba1⁺ area normalized by DAPI⁺ area around bare, BDNF-coated, and TAB-coated groups at 1 day and 1 week postimplantation, respectively. (**E**) Representative confocal images of astrocytic expression surrounding the fiber. Average fluorescent intensity quantifying the presence of \$100A10 at 1 day (**F**) and 1 week (**G**) postimplantation. Average fluorescent intensity quantifying the presence of C3 at 1 day (**H**) and 1 week (**I**) postimplantation. Scale bars, 100 μm. [n = 3 for (C), (D), (F), (H), and (I) and n = 4 for (G)] (*P < 0.05, **P < 0.01). ns, not significant. a.u., arbitrary units.

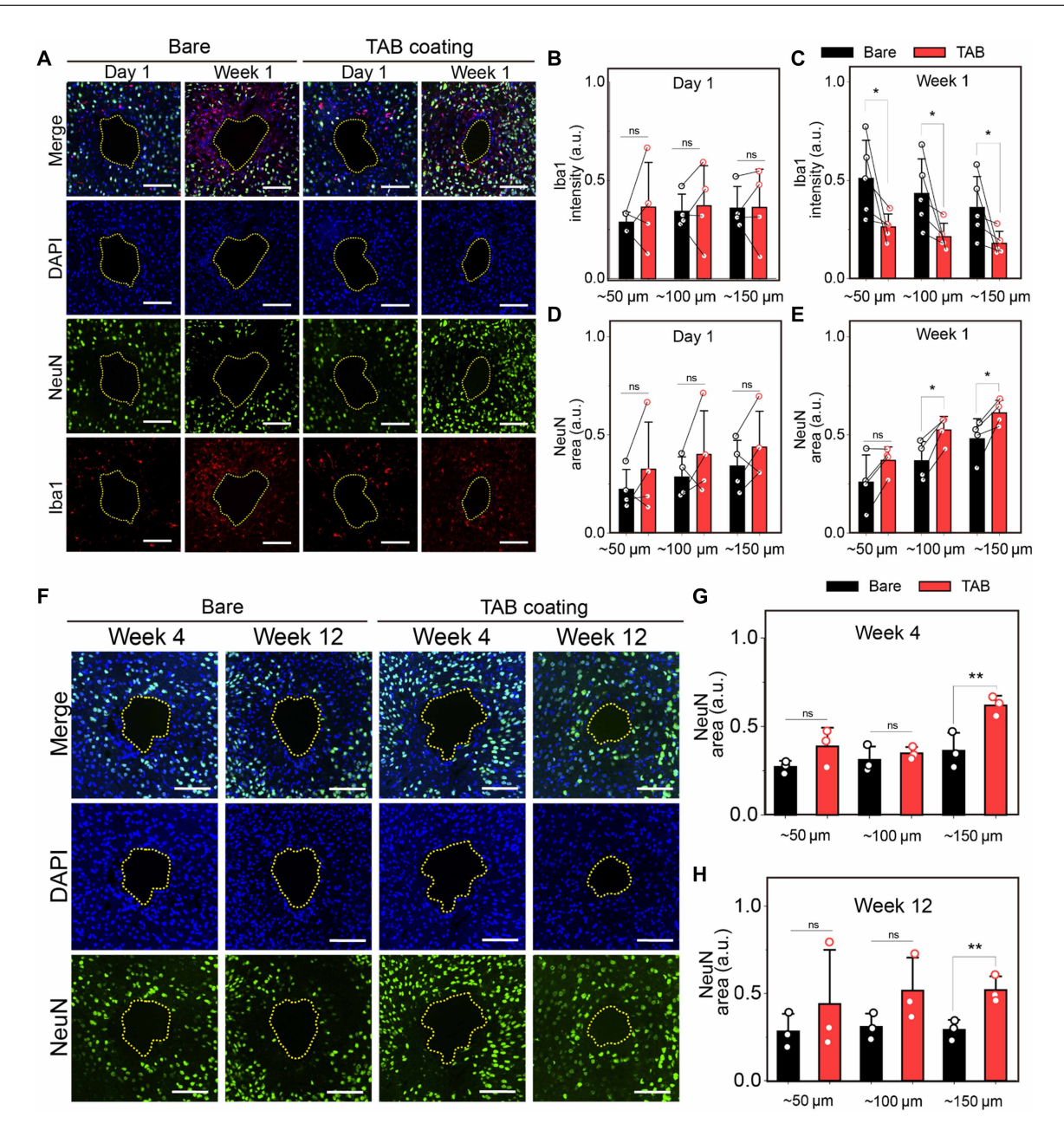


Fig. 5. In vivo evaluation of neuronal survival at the device-tissue interface. (**A**) Representative confocal images of neuronal survival and glial scarring around the fiber at 1 day and 1 week postimplantation. Average fluorescent intensity quantifying the presence of Iba1 at 1 day (**B**) and 1 week (**C**) postimplantation. Area(%) quantifying the presence of NeuN at 1 day (**D**) and 1 week (**E**) postimplantation. (**F**) Representative confocal images of neuronal survival in 4 and 12 weeks postimplantation. Area(%) quantifying the presence of NeuN at 4 weeks (**G**) and 12 weeks (**H**) postimplantation around the fiber. Scale bars, 100 μm. [n = 4 for (B), (C), (D), (E), (G), and (H) and n = 5 for (C)] (*P < 0.05, **P < 0.01). ns, not significant.

postimplantation. The TAB-applied group shows decreased Iba1 expression at week 1 postimplantation compared to the bare group (Fig. 5, B and C). Moreover, most microglia surrounding TAB-coated fibers did not exhibit full activation by day 1 postimplantation, whereas those around bare fibers reached activation levels by day 1 comparable to those at week 1 (fig. S14B). Reduced activation of microglia in the TAB group increases access for surviving neurons in the vicinity, thereby the NeuN⁺ area is larger at the TAB interface than the bare at 1 week postimplantation (Fig. 5, D and E). In other words, our device facilitates the restoration of the implant site

to a healthy state and enhances the survival of neurons in the effective region for recording spiking activities. The NeuN expression on day 1 postimplantation does not show a statistical difference between TAB-coated fibers and bare fibers, indicating that the neurotrophic effect takes several days to become effective. The changes in the immune response and neuronal survival rate in the early phases of implantation are critical in the outcome of the long-term implants. The efficacy of TAB-applied fiber is further validated to have a long-term advantage over the bare device by 4-week and 12-week IHC results (Fig. 5F). In Fig. 5 (G and H), NeuN⁺ area% is larger at

the TAB-coated interface than the bare interface both in 4 and 12 weeks postimplantation, as is in the earlier period. Therefore, improved neuronal survival at the TAB-coated interface is distinct at various points of postimplantation. This implies that once the TAB coating adapts the implant site into a neuron-friendly environment, the neurons that survived the short-term implantation damage can remain functional in the long term. The TAB coating preserves the temporal window for BDNF to mitigate the FBR in the short term, thereby contributing to a reduction in chronic FBR. Then, the TAB coating brings a synergic effect with flexible polymer-based fibers, which minimize the long-term mechanical damage to the neighboring neurons.

Long-term electrophysiology recording of endogenous spike activities

We further investigated the neuron-friendly biochemical effect of TAB-applied flexible fiber by in vivo e-phys recording in the extended period of time. The long-term survival of neurons at the devicetissue interface is crucial for the functionality of an invasive neural interface deciphering the chronic status of the brain region (Fig. 6A). It is especially crucial when recording neuronal spike activities since the spike amplitude is inversely proportional to the distance between the recording electrode and the soma. The improved survival of neurons at the TAB interface allows a high-quality recording of endogenous spike activities in mouse hippocampus at 10 months postimplantation (Fig. 6B). The chronic electrophysiology results show that the neuron-friendly TAB coating combined with flexible polymer provides protection for neural tissue at the implant site, and its synergistic effect persists for almost a lifetime of a mouse. The endogenous neural activities in the CA1 region have been monitored bimonthly, and recorded spike signals are analyzed to evaluate the operation of the device. We show that a TAB-applied fiber extended the life span of the fiber device, which allows high-quality recording of single unit activity from 6 to 12 months (Fig. 6, C and D). The shape of the detected waveform, principal components analysis (PCA), and interspike interval histogram suggest that the bare fiber device is no longer operational in recording spike activities after 6 months (Fig. 6, C and E, and fig. S15). Reduced capability to capture neuronal spiking activities in bare neural fibers suggests that the neural tissue around the bare fiber has been altered by neuroinflammation as a part of FBR. Loss of ability to record single neuron activity is attributed to the formation of scar tissue encapsulating the microelectrode and the death of neurons at the device-tissue interface. On the other hand, TAB-applied fiber effectively reduces FBR and is eligible to track endogenous spiking activities for up to 12 months, with no substantial deterioration in the signal (Fig. 6, B, D, and F, and fig. S16). Last, we analyzed the characteristics of recorded spiking units during the statistically analyzable 8-month implantation for comparison of bare and TAB-coated fibers. The number of detected spike units per electrode has been maintained in TAB-coated fibers while it decreased in bare fibers (Fig. 6G). Furthermore, there is no sign of deterioration in the amplitude of the neuronal spikes detectable with TAB-coated fibers (Fig. 6H), which leads to an excellent signal-tonoise ratio (SNR) consistent over time (Fig. 6I). The long-term seamless integration of our device and the target tissue is attributed to the stealthy properties of our device leaving the implant site with little damage over 12 months of implantation. The results suggest that our device can provide a lifelong recording of the target brain without damaging the neurons at the implant site.

DISCUSSION

In this study, we applied a TAB coating to flexible neural fiber to enhance the long-term stability and recording fidelity. By integrating BDNF immobilization with a lubricated surface using a partial silanization technique, we successfully addressed critical challenges such as FBR, glial encapsulation, micromotion-induced tissue damage, and biofouling, which traditionally limit the life span and effectiveness of neural implants. The TAB coating was designed to provide a dual-functional approach: promoting selective interaction with neurons and astrocytes while simultaneously preventing nonspecific adhesion of biosubstances, especially immune-related substances. The immobilized BDNF on the device surface facilitated targeted neuronal interactions by binding to TrkB receptors, which enhanced neuronal survival and promoted neuroprotective astrocyte activity. At the same time, the lubricant layer effectively repelled blood and plasma proteins, reducing immune cell adhesion and activation. This strategy not only improved cell selectivity but also mitigated the inflammatory responses commonly associated with implanted neural devices. These TAB coating's biochemical effects contributed to enhanced neuronal survival and prevented the formation of fibrotic tissue at the implant site. Furthermore, in vivo histological analysis confirmed that the TAB-coated fibers facilitated higher retention of NeuN⁺ neurons, indicating improved long-term neural viability at the device-tissue interface. In addition to its biochemical benefits, the TAB coating also provides mechanical advantages. The lubricated surface reduced insertion force and mechanical stress, minimizing acute implantation trauma and preventing chronic micromotioninduced damage. As a result, TAB-coated neural fibers exhibited high-fidelity neural signal recording for over a year, whereas conventional uncoated fibers showed substantial signal degradation after just 6 months. The ability to maintain long-term signal integrity underscores the importance of combining mechanical adaptability with biochemical compatibility for effective neural interfaces. Overall, this study presents an innovative bioactive lubricated surface that enables seamless integration of neural implants with brain tissue while mitigating immune responses and improving neuronal interactions. By enhancing both biocompatibility and mechanical stability, TABcoated neural devices offer a promising solution for long-term, highresolution neural signal recording, making them highly suitable for applications in brain-machine interfaces, neuroprosthetics, and neuromodulation therapies.

MATERIALS AND METHODS

Multifunctional fiber fabrication

The multifunctional fiber interfaces were thermally drawn from a PC/PMMA/PC polymer preform, along with tungsten microwires. Schematic illustration of the preform preparation is shown in fig. S17. The preform was prepared by first wrapping a 6.35-mm-diameter PC rod (Goodfellow) with a PMMA film (Goodfellow) with a thickness of 50 μm to form a 5.5-mm-thick PMMA cladding around the PC optical core. The PC/PMMA rod was baked in a vacuum oven at 150°C for 30 min for consolidation. Three channels of 4-mm depth were made along the rod by machining. Following the machining, the PC/PMMA rod was wrapped with a 100- μm -thick PC film (Goodfellow) to make the final preform diameter of 24 mm. Two of the channels were threaded with 25- μm tungsten wires before TDP. Each end of the threaded wires was connected to a spool, which was fixed at the top of the custom drawing tower. The thermoplastic

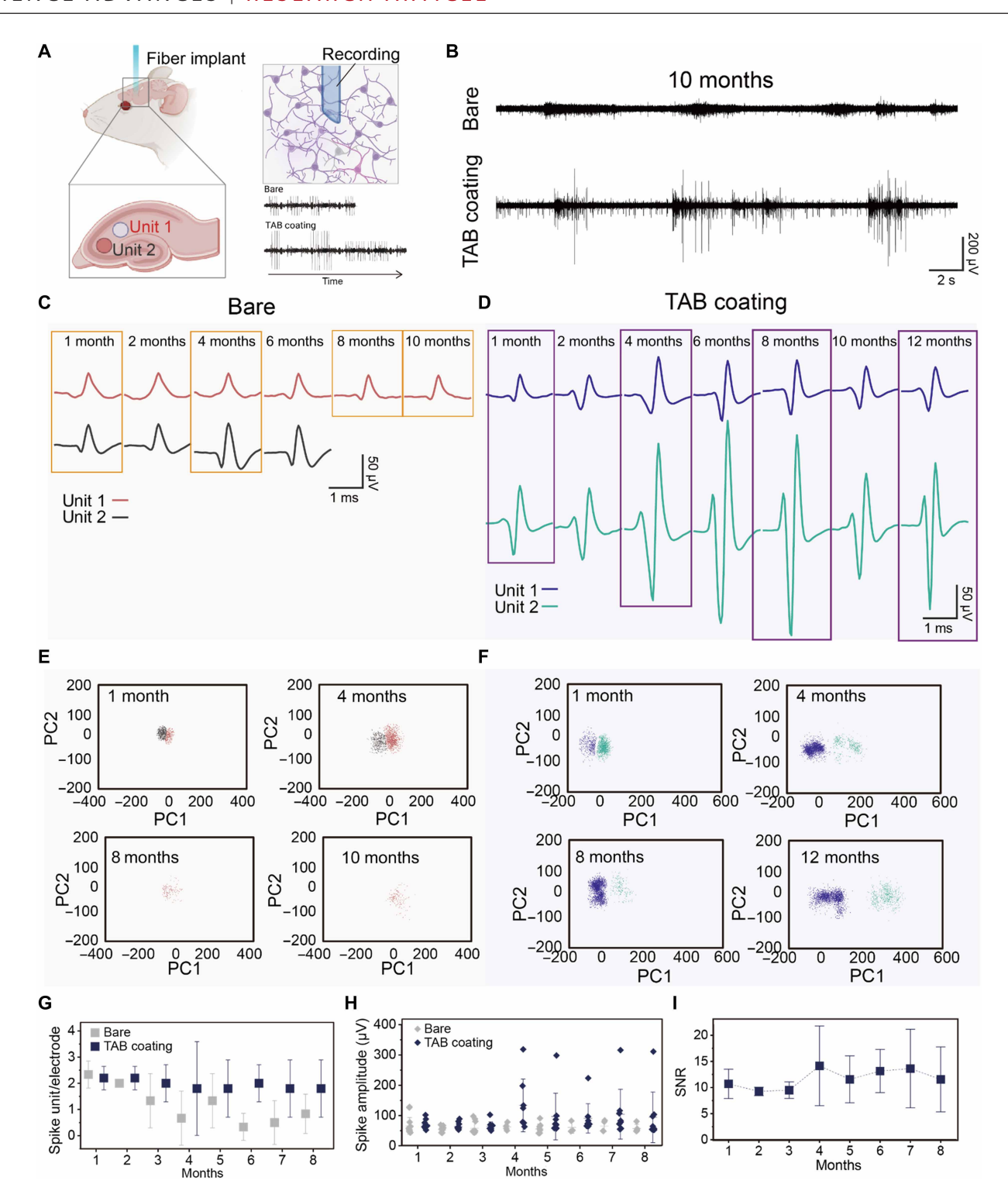


Fig. 6. Long-term electrophysiology recording of endogenous spike activities. (A) Schematic illustration of signal recording. (B) Electrophysiology recording of endogenous mouse hippocampal CA1 activity using bare and TAB-applied fiber at 10 months postimplantation. (\mathbf{C} and \mathbf{D}) Recoding profile of sorted single-neuron action potentials (spikes) with a bare device and TAB-applied fiber. (\mathbf{E} and \mathbf{F}) PCA clusters at 1, 4, 8, and 10 months postimplantation of a bare device and 1, 4, 8, and 12 months postimplantation of the TAB-applied fiber. (\mathbf{G}) The number of recorded spike units per electrode (n = 5 for TAB coating, n = 6 for bare, n = 6 for bare, n = 6 for bare, n = 6 for bare and n = 6 for bare and n = 6 for bare and n = 6 for table coating. (n = 6) SNR of electrophysiology recording with TAB-applied fiber (n = 8). n = 6 value is calculated from one-way repeated measures ANOVA, n = 6 for table coating. (n = 6) SNR of electrophysiology recording with TAB-applied fiber (n = 8). n = 6 value is calculated from one-way repeated measures ANOVA, n = 6 for table coating.

polymer preform was codrawn with the wires at 175°C, at a feed speed of 0.6 mm/min with different capstan speeds (3.6, 4.2, 6, and 9.6 m/min)

Characterization of the multifunctionality of fiber device

The flexural rigidity of the multifunctional fibers was calculated from modulus measured by a dynamic mechanical analyzer (Anton Paar) within the frequency range 0.01 to 10 Hz (fig. S18). Before in vivo experiments, optical, microfluidic, and electrical performances have been evaluated. The fiber was connected to optical ferrule, metal wire, and tubing for the connection (fig. S1). To measure the optical transmission loss, the fiber was connected to a 465-nm blue laser (LIOG473-80-A1, RWD) via an optical patch cord, and the optical transmission was measured with optical power meter (S121C and PM100D, Thorlabs). The microfluidic channel was characterized via infusion of the methylene blue aqueous solution into 0.6% agarose gel at a speed of 100 nl/min. The fluid return rate was calculated by measuring the weight of solution collected at the tip after infusion at a rate of 1 μ l/min.

Synthesis of TAB coating

Oxygen plasma treatment (70 W, 2 min) was applied to the substrates using a plasma system (COVANCE, Femto Science, Korea) to generate hydroxyl groups on their surfaces. Subsequently, the substrates and a 200-µl droplet of PFS (Sigma-Aldrich, Germany) were placed inside a desiccator. A vacuum pump was activated until the pressure inside the desiccator reached 0.1 MPa. The silanization reaction was then carried out at room temperature for 2 hours. Afterward, the substrates were heated in an oven at 60°C for at least 12 hours. To remove noncovalently attached PFS molecules, the silanized substrates were sonicated in DI water for 10 min. For partial silanization of the fully fluorinated substrates, a secondary oxygen plasma treatment (30 W, 5 s) was gently applied to the PFS functionalized samples, selectively removing silanized PFS from the surface. The samples were then placed in a desiccator along with a 200-µl droplet of APTES (Sigma-Aldrich, Germany) under a vacuum of 0.1 MPa for 2 hours. The partially silanized substrates were subsequently annealed in an oven at 60°C for at least 12 hours and sonicated in DI water for 10 min. To covalently immobilize BDNF onto the partially silanized substrates, EDC/NHS chemistry was used to conjugate the amine groups of APTES with the carboxyl groups of BDNF. A solution containing BDNF (100 ng/ml; PeproTech, Thermo Fisher, USA), EDC, and NHS was prepared in 0.1 M MES buffer (pH 5.5). The partially silanized substrates were immersed in this BDNF solution at 4°C for 24 hours. Following the reaction, the substrates were thoroughly washed with 0.1 M MES buffer and DI water. Last, the fluoro-silanized substrates were infused with a PFPE lubricant (Krytox 101, DuPont, USA), and excess lubricant was removed by tilting the substrates.

Antifouling evaluation

Defibrinated horse blood (Kisanbio, Korea) was used to conduct the blood fouling test on both bare and TAB-coated multifunctional fibers. For this test, 10- μ l droplets of blood were placed on each sample group, and the extent of blood staining was quantified using ImageJ software. Next, we evaluated the protein adhesion test with plasma proteins (albumin and fibrinogen). Alexa Fluor 488–conjugated bovine serum albumin (A13100) and human plasma fibrinogen (F13191) were obtained from Invitrogen. To assess the ability of the

TAB-coated group to resist plasma protein adhesion, bare and TAB-coated samples were immersed in 5 ml of aqueous protein solutions (1 mg/ml) and incubated at 37°C for 24 hours. After incubation, the specimens were rinsed with DI water and air-dried at room temperature. Protein adsorption on the poly(dimethylsiloxane) (PDMS) was then analyzed using an inverted fluorescence microscope (IX81, Olympus, Japan) and quantified with the ImageJ/FIJI software.

Characterization of TAB coating

The CA and sliding angle (SA) under static conditions were measured on both bare and TAB-coated PC substrates with a CA measurement system equipped with a dynamic image capture camera (SmartDrop Standard Plus, FEMTOBIOMED Inc.). For CA measurements, 10-µl droplets of various liquids (DI water, defibrinated horse blood from Kisan Bio, DMSO, acetone, ethylene glycol, and ethanol from Sigma-Aldrich) were deposited on the substrates. The SA for each liquid was recorded as the substrate was tilted at a rate of one degree per second until the droplet began to roll. Similarly, CAs and SAs were determined for a range of versatile materials including glass, wafer, PDMS, Ecoflex, polyvinyl chloride, polypropylene, and aluminum (AL5052) both in their bare state and after TAB coating. In addition, XPS (PHI 5000 VersaProbe, ULVAC PHI) equipped with an Al K-alpha x-ray source (spot size: $100~\mu m^2$) was used to analyze the surface chemical composition.

Measurement of load during insertion and retraction

The load exerted on the phantom brain (0.6% agarose gel) during insertion and retraction of the fiber device was measured using a load cell (LTS-50GA, Kyowa) connected to a strain amplifier (DPM-911B, Kyowa). The fiber was actuated with a high-resolution dc motor actuator (M-111.1DG, Physik Instrumente), and the load exerted by the fiber was measured every 100 ms. The insertion and retraction speeds of the fiber were both set at 0.1 mm/s, and the maximum insertion depth was 2.5 mm. To study stress relaxation behavior after stopping insertion, measurements were taken until the load plateaued for at least 3 min.

MD simulations

MD simulations were conducted to investigate the interfacial behavior of lubricant molecules on PFS/APTES-coated surface. All MD simulations were performed with COMPASS III forcefield (46). The van der Waals interactions were treated using an atom-based summation method with a cutoff distance of 12.5 Å, and electrostatic interactions were calculated using a particle-particle particle-mesh method with accuracy of 0.001 kcal/mol. The NVT (constant number of particle, volume, and temperature) ensemble (canonical ensemble) was simulated at 310.15 K with a 1-fs time step using a Berendsen thermostat (47) for 310 ns. After the NVT simulations, the analyses of the concentration profiles were performed from 300 to 310 ns.

Density functional theory calculations

Density functional theory calculations were carried out using the DMol3 program (48) to investigate the electrostatic potential isosurface of molecules and binding energies of lubricant with TPFS or APTES molecule. The exchange-correlation energy was treated using generalized gradient approximation with Perdew-Burke-Ernzerhof functional (49). Spin-polarized calculations were conducted, and orbital cutoff was set at 4.6 Å. The dispersion corrections were applied using the Tkatchenko-Scheffler method (50). All electron relativistic

core treatments and double numerical plus polarization (version 4.4) basis set were adopted to describe the core electrons and the atomic orbital basis set, respectively. For the geometry optimization, the convergence criteria of energy, force, displacement, and self-consistent field were set to 1×10^{-5} Ha, 0.002 Ha/Å, 0.005 Å, and 1×10^{-6} Ha, respectively.

The binding energies of the lubricant with PFS or APTES molecule were calculated by following equation

Binding energy =
$$E_{\text{total}} - E_{\text{lubricant}} - E_{\text{PFS or APTES}}$$
 (1)

where E_{total} , $E_{\text{lubricant}}$, and $E_{\text{PFS or APTES}}$ are the total energy of lubricant with PFS or APTES molecule, the energy of lubricant molecule, and the energy of PFS or APTES molecule, respectively.

In vitro biocompatibility evaluation

To assess cytotoxicity, both bare and TAB-coated multifunctional fibers were prepared. A two-chamber transwell system with an 8-µm pore size (Corning) was then used to analyze cell viability and morphological changes. The fibers were placed onto the transwell insert, and NIH-3T3 fibroblast cells (0.5×10^5 cells/ml) were cultured in 2 ml of Dulbecco's modified Eagle's medium containing 10% fetal bovine serum and 1% penicillin-streptomycin. Cell viability was determined using a Live/Dead kit (L3224, Invitrogen, USA) following the manufacturer's protocol, and images were captured with an inverted fluorescence microscope (IX81, Olympus, Japan) at ×10 magnification. Morphological changes were assessed by calculating the aspect ratio, defined as the ratio of the major cell axis to the minor cell axis. For visualization purposes, the actin cytoskeleton of the fibroblasts was stained with Alexa Fluor 594-conjugated phalloidin (Thermo Fisher Scientific, Pittsburgh, PA, USA). The fibroblast morphology was then examined using a confocal microscope (LSM 980, Carl Zeiss, Oberkochen, Germany) and analyzed with the ImageJ/FIJI software.

In vitro selective adhesion test

To assess the selective adhesion of neuronal cells to the TAB-coated substrate, primary hippocampal cells were extracted from a mouse brain. The extracted cells were cultured in neurobasal medium (21103049, Gibco, USA) supplemented with 1% GlutaMAX-1 (S001-01, Welgene, Korea) and 1% penicillin-streptomycin (LS202-02, Welgene, Korea). For the adhesion test, the cells were seeded onto the TAB-coated cell culture dish at a density of 0.5×10^6 cells/ml and maintained in an incubator at 37°C with 5% CO₂. After 3 days of culture, cell attachment was confirmed under an optical microscope. Subsequently, samples were fixed with 4% paraformaldehyde (PFA) for 20 min and permeabilized with 0.1% Triton X-100 in phosphate-buffered saline (PBS) for 10 min. Nonspecific binding was blocked by incubating the cells in 2% bovine serum albumin in PBS for 1 hour at room temperature. Cells were then incubated overnight at 4°C with the following primary antibodies diluted in blocking solution: rabbit anti-glial fibrillary acidic protein (GFAP; G3893, Sigma-Aldrich, 1:500, astrocyte marker), mouse anti-NeuN (NAB377, Sigma-Aldrich,1:500, neuronal marker), and goat anti-Iba1 (SAB2702364, Sigma-Aldrich,1:500, microglial marker). The following day, after through PBS washing, cells were incubated for 1 hour at room temperature with species-specific secondary antibodies conjugated to fluorescent dyes: Alexa Fluor 488-conjugated goat anti-rabbit immunoglobulin G (IgG; for GFAP), Alexa Fluor 594-conjugated goat anti-mouse IgG (for NeuN), and Alex Fluor

647–conjugated donkey anti-goat IgG (for Iba1), each diluted 0:500 in blocking duffer. All fluorescence imaging was performed using a confocal microscope (LSM 900, Carl Zeiss, Germany).

Enzyme-linked immunosorbent assay

To quantify the levels of MMP-9, TNF-α, IL-6, and IL-8, an in vitro ELISA assay was performed using commercial ELISA kits. Cells were cultured under specific experimental conditions, and the culture supernatants were collected at the designated time points. The collected supernatants were centrifuged at 1500 rpm for 10 min to remove any debris and then stored at -80°C until analysis. The concentrations of MMP-9, TNF-α, IL-6, and IL-8 were measured using corresponding ELISA kits (manufacturer and catalog numbers). The assay was conducted according to the manufacturer's instructions. Briefly, 100 µl of standards and samples was added to the precoated wells and incubated at 37°C for the recommended duration. Following incubation, the wells were washed with the provided wash buffer to remove unbound substances. Subsequently, 100 µl of the detection antibody conjugated with horseradish peroxidase was added and incubated at room temperature for the specified time. After another washing step, the substrate solution was added to each well and incubated in the dark for color development. The reaction was stopped using a stop solution, and the optical density (OD) was measured at 450 nm using a microplate reader. The concentrations of MMP-9, TNF- α , IL-6, and IL-8 in the samples were determined by interpolating the OD values against a standard curve generated from known concentrations. All experiments were performed in triplicate to ensure reproducibility, and statistical analysis was conducted to evaluate significant differences among experimental groups.

Real-time PCR

Total RNA extraction from cells and tissues was performed using TRIzol (Invitrogen) following the manufacturer's protocol. The extracted RNA was quantified using a NanoDrop 2000 spectrophotometer (Thermo Fisher Scientific). cDNA synthesis was performed using AccuPower CycleScript RT Premix (Bioneer) following the manufacturer's instructions, using a T-100 Thermal Cycler (Bio-Rad). Subsequently, PCR was conducted in a T100 Thermal Cycler (Bio-Rad) using a primer set and HiPi Plus 5 × PCR premix (Elpisbio), followed by agarose gel electrophoresis. qPCR was performed using the StepOne Plus Real-Time PCR System (Applied Biosystems) using cDNA, primer set, and SYBR Green PCR mix (Applied Biosystems), followed by melting curve analysis. For the characterization of the blood-brain barrier (BBB) chip model, the total RNA was extracted using the Universal RNA Extraction Kit (Bioneer). Subsequently, cDNA was synthesized through reverse transcription using the AccuPower RT PreMix & Master Mix (Bioneer). This process was conducted in a T100 Thermal Cycler (Bio-Rad). The realtime PCR analysis was performed using the SYBR Green Realtime PCR Master Mix (TOYOBO) with a CFX Connect Real-Time PCR Detection System (Bio-Rad). Data analysis was performed using the comparative Ct (2- $\Delta\Delta$ Ct) method, and the results were normalized to the expression of the corresponding glyceraldehyde 3-phosphate dehydrogenase. Primer sequences are provided in table S1.

FBR evaluation under in vivo conditions

A subcutaneous implantation model was used using 7-week-old female institute of cancer research (ICR) mice (n = 3 per group). Mice were anesthetized using inhalation anesthesia (isoflurane in

oxygen, 0.5 liters/min O_2 flow rate), and the dorsal right side of each mouse was shaved and sterilized with povidone iodine and 70% ethanol. A small skin incision (~1 cm) was made, and a 0.5-cm-long neural fibers (with or without TAB coating) were gently inserted into the subcutaneous space using sterile forceps. The incision was closed using 5-0 sutures. After 7 days, mice were euthanized, and the implanted regions, including surrounding tissues, were harvested and fixed with 10% PFA overnight. Tissues were then processed for paraffin embedding and sectioned for histological analysis, including H&E staining and Masson's Trichrome stain (MT) staining to assess immune cell infiltration and collagen deposition around the implant site.

In vivo electrophysiology

All surgical procedures were performed in accordance with protocols approved by the Institutional Animal Care and Use Committee (KA2023-139-v1) at Korea Advanced Institute of Science and Technology. Eight- to10-week male B6 mice (Koatech, South Korea) were anesthetized with isoflurane (4% induction, 1 to 2% maintenance) for implantation surgery and electrophysiology recording. The neural fiber is implanted in a mouse hippocampal region [mediolateral (ML), -1.1; anteroposterior (AP), -1.85; dorsoventral (DV), -1.1]. The implanted neural fiber is secured to the skull along with reference and ground electrodes with superbond (C&B super bond, Sun Medical) and dental cement (Ortho-jet, Lang Dental). The electrophysiology recording was conducted following 1 week of postoperative recovery. The neural signal was recorded with the Lab Rat electrophysiology system [Tucker Davis Technologies (TDT)]. Neural probes were connected to the Lab Rat via ZIF-Clip analog headstage (TDT). The neural stream was band-pass filtered with a 300- to 5000-Hz filter to acquire high-frequency spike signals. For optogenetic stimulation, 465-nm blue light (54 mW/mm², 1 Hz, 5-ms pulse width) was delivered to the hippocampal region in the Thy1-ChR2-eYFP mouse brain under anesthesia. For CNQX delivery, the microfluidic channel was connected to the tubing (E-3603, Tygon) and fixed with ultraviolet resin. A total of 0.01 mM CNQX (C127, Sigma-Aldrich) solution in artificial cerebrospinal fluid was loaded in a syringe (Gastight 700 series, Hamilton) and injected with a syringe pump (RWD). Following the surgery, every mouse was individually housed in a 12-hour light/dark cycle at 22°C with ad libitum access to food and water.

Immunohistochemistry

To compare the implantation damage of TAB-coated fibers to that of bare fibers, fibers were implanted into contralateral sites of the same mouse brain. After 1 day, 1 week, 4 weeks, and 12 weeks of fiber implantation, mice underwent transcardiac perfusion with PBS, followed by 4% PFA. The brains were dissected and fixated overnight in 4% PFA at 4°C. For cryoprotection, brains were immersed in 30% sucrose solution for a few days until fully equilibrated. The brains were then embedded in optimal cutting temperature (OCT) compound (Tissue-Tek, Sakura) and froze at −20°C. Horizontal frozen sections (40 µm thick) were prepared at depth-matched anatomical regions for a fair comparison of implantation damage between TABcoated and bare fibers. Sections were rinsed in PBS before staining. For blocking of nonspecific binding and permeabilization, the sections were incubated in 0.3% Triton X-100 (Sigma-Aldrich) and 5% normal donkey serum (Abcam) solution for 1 hour. The sections were then incubated overnight at room temperature with primary

antibodies: rabbit anti-MMP-9 (1:100; ab228402, Abcam), goat Iba1 (1:500; ab5076, Abcam), goat anti-S100A10 (10 μg/ml; AF2377, R&D Systems), rat anti-C3 (1:500; NB200-540, Novus Biologicals), rabbit anti-GFAP (1:250; ab68428, Abcam), and rat anti-NeuN (1:1000; ab279297, Abcam. The sections were rinsed with PBS and incubated for 2 hours with secondary antibodies: donkey anti-rabbit Alexa Fluor 488 (1:500; ab150064, Abcam), donkey anti-goat IgG Alexa Fluor 594 (ab150132, Abcam), donkey anti-goat IgG Alexa Fluor 488 (ab150129, Abcam), donkey anti-rat IgG Alexa Fluor 488 (Invitrogen, A21208), and donkey anti-rabbit IgG Alexa Fluor 594 (Abcam, ab150076). After rinsing, the sections were mounted on coated slide glass and counterstained with DAPI (4',6-diamidino-2-phenylindole; Vectashield H-1200, Vector Laboratories). The sections were imaged with a laser scanning confocal microscope (C2, Nikon). Acquired images were analyzed with ImageJ software. For day 1 MMP-9 analysis, the area percentage of MMP-9⁺ regions surrounding the fiber trace was measured within a 630 µm-by-630 µm region of interest (ROI), centered on the fiber trace. For week 1 Iba1 analysis, the Iba1⁺ area was normalized to the DAPI⁺ area within the same 630 μm-by-630 μm ROI centered on the fiber trace. For S100A10 and C3 analysis, the mean intensities of these astrocyte subtype-specific proteins within GFAP-colocalized regions were compared across varying distances (50, 100, and 150 µm) from the fiber trace (51-54). To compare Iba1 and NeuN expressions at regions located at varying distances from the fiber, the mean intensity of Iba1 and the area percentage of NeuN were calculated. The circularity of glial cells was quantified with ImageJ software, using particle analyze function on confocal images.

Spike sorting

Neuronal spike activities are detected and sorted with commercially available offline sorter (Plexon). The spike activities were detected on the basis of the amplitude thresholding, which remained unchanged for each channel. The waveforms were aligned to the largest peak after threshold crossing and sorted with scanning k-means clustering algorithms. The number of clusters was counted as the number of spike units provided that the calculated L ratio of two-dimensinal clusters is less than 0.05. L ratios and isolation distances were calculated with the offline sorter.

SNR calculation

SNR was calculated with MATLAB, according to the following equation

$$SNR = \frac{A}{\sigma} \tag{2}$$

where A is the maximum peak-to-valley amplitude of the mean spike waveform, and σ is the SD of the background noise on the same channel, computed via the median absolute deviation.

Statistical analysis

GraphPad Prism software (GraphPad Software Inc., USA) and Origin (OriginLab Corporation) were used to carry out statistical analysis. The unpaired t test, ordinary two-way analysis of variance (ANOVA), and Tukey's multiple comparisons test were used to evaluate variations between groups, with individual variances calculated for each comparison. The levels of statistical significance are represented in the figures as follows: *P < 0.05, **P < 0.01, ***P < 0.001, and ****P < 0.0001.

Supplementary Materials

The PDF file includes:

Figs. S1 to S18 Tables S1 to S3 Legend for movie S1

Other Supplementary Material for this manuscript includes the following:

REFERENCES AND NOTES

- P. W. Sayyad, S.-J. Park, T.-J. Ha, Bioinspired nanoplatforms for human-machine interfaces: Recent progress in materials and device applications. *Biotechnol. Adv.* 70, 108297 (2024).
- W. Dong, Y. Wang, Y. Zhou, Y. Bai, Z. Ju, J. Guo, G. Gu, K. Bai, G. Ouyang, S. Chen, Soft human-machine interfaces: Design, sensing and stimulation. *Int. J. Intell. Robot. Appl.* 2, 313–338 (2018).
- E. Musk, An integrated brain-machine interface platform with thousands of channels. J. Med. Internet Res. 21, e16194 (2019).
- M. H. Malekoshoaraie, B. Wu, D. D. Krahe, Z. Ahmed, S. Pupa, V. Jain, X. T. Cui, M. Chamanzar, Fully flexible implantable neural probes for electrophysiology recording and controlled neurochemical modulation. *Microsyst. Nanoeng.* 10, 91 (2024).
- A. Gupta, N. Vardalakis, F. B. Wagner, Neuroprosthetics: From sensorimotor to cognitive disorders. Commun. Biol. 6, 14 (2023).
- M. S. Okun, Deep-brain stimulation for Parkinson's disease. N. Engl. J. Med. 367, 1529–1538 (2012).
- C.-H. Chiang, S. M. Won, A. L. Orsborn, K. J. Yu, M. Trumpis, B. Bent, C. Wang, Y. Xue, S. Min, V. Woods, Development of a neural interface for high-definition, long-term recording in rodents and nonhuman primates. Sci. Transl. Med. 12, eaay4682 (2020).
- M. J. Vansteensel, E. G. Pels, M. G. Bleichner, M. P. Branco, T. Denison, Z. V. Freudenburg, P. Gosselaar, S. Leinders, T. H. Ottens, M. A. Van Den Boom, Fully implanted brain-computer interface in a locked-in patient with ALS. N. Engl. J. Med. 375, 2060–2066 (2016).
- K. A. Johnson, M. S. Okun, K. W. Scangos, H. S. Mayberg, C. de Hemptinne, Deep brain stimulation for refractory major depressive disorder: A comprehensive review. Mol. Psychiatry 29, 1075–1087 (2024).
- P. Limousin, T. Foltynie, Long-term outcomes of deep brain stimulation in Parkinson disease. Nat. Rev. Neurol. 15, 234–242 (2019).
- J. K. Krauss, N. Lipsman, T. Aziz, A. Boutet, P. Brown, J. W. Chang, B. Davidson, W. M. Grill, M. I. Hariz, A. Horn, M. Schulder, A. Mammis, P. A. Tass, J. Volkmann, A. M. Lozano, Technology of deep brain stimulation: Current status and future directions. *Nat. Rev. Neurol.* 17, 75–87 (2021).
- C. A. Chestek, V. Gilja, P. Nuyujukian, J. D. Foster, J. M. Fan, M. T. Kaufman, M. M. Churchland, Z. Rivera-Alvidrez, J. P. Cunningham, S. I. Ryu, Long-term stability of neural prosthetic control signals from silicon cortical arrays in rhesus macaque motor cortex. J. Neural Eng. 8, 045005 (2011).
- E. Redolfi Riva, S. Micera, Progress and challenges of implantable neural interfaces based on nature-derived materials. Bioelectron. Med. 7, 6 (2021).
- S. Zhao, X. Tang, W. Tian, S. Partarrieu, R. Liu, H. Shen, J. Lee, S. Guo, Z. Lin, J. Liu, Tracking neural activity from the same cells during the entire adult life of mice. *Nat. Neurosci.* 26, 696–710 (2023)
- W. Jeon, J. M. Lee, Y. Kim, Y. Lee, J. Won, S. Lee, W. Son, Y. H. Koo, J. W. Hong, H. Gwac, Structurally aligned multifunctional neural probe (SAMP) using forest-drawn CNT sheet onto thermally drawn polymer fiber for long-term in vivo operation. *Adv. Mater.* 36, 2313625 (2024).
- J. W. Salatino, K. A. Ludwig, T. D. Kozai, E. K. Purcell, Glial responses to implanted electrodes in the brain. *Nat. Biomed. Eng.* 1, 862–877 (2017).
- S. M. Wellman, T. D. Kozai, Understanding the inflammatory tissue reaction to brain implants to improve neurochemical sensing performance. ACS Chem. Neurosci. 8, 2578–2582 (2017).
- C. Marin, E. Fernández, Biocompatibility of intracortical microelectrodes: Current status and future prospects. Front. Neuroeng. 3, 1212 (2010).
- N. Sharafkhani, A. Z. Kouzani, S. D. Adams, J. M. Long, G. Lissorgues, L. Rousseau, J. O. Orwa, Neural tissue-microelectrode interaction: Brain micromotion, electrical impedance, and flexible microelectrode insertion. J. Neurosci. Methods 365, 109388 (2022).
- 20. A. Noguchi, Y. Ikegaya, N. Matsumoto, In vivo whole-cell patch-clamp methods: Recent technical progress and future perspectives. *Sensors* **21**, 1448 (2021).
- W. Chen, J. Sheng, J. Guo, G. Peng, J. Hong, B. Li, X. Chen, K. Li, S. Wang, Cytokine cascades induced by mechanical trauma injury alter voltage-gated sodium channel activity in intact cortical neurons. *J. Neuroinflammation* 14, 73 (2017).
- T.Y. Kim, S. An, Y. Kim, S. Y. Han, J. Lee, K. Park, S. Kim, J. Park, S. A. Kim, J. J. Chung, Lubricant-infused polymeric interfaces: A stretchable and anti-fouling surface for implantable biomaterials. *Adv. Funct. Mater.* 34, 2312740 (2024).

- J. Park, Y. Lee, T. Y. Kim, S. Hwang, J. Seo, Functional bioelectronic materials for long-term biocompatibility and functionality. ACS Appl. Electron. Mater. 4, 1449–1468 (2022).
- T. M. O'Shea, A. L. Wollenberg, J. H. Kim, Y. Ao, T. J. Deming, M. V. Sofroniew, Foreign body responses in mouse central nervous system mimic natural wound responses and alter biomaterial functions. *Nat. Commun.* 11, 6203 (2020).
- A. Carnicer-Lombarte, S.-T. Chen, G. G. Malliaras, D. G. Barone, Foreign body reaction to implanted biomaterials and its impact in nerve neuroprosthetics. Front. Bioeng. Biotechnol. 9, 622524 (2021).
- Y. Lee, H. Shin, D. Lee, S. Choi, I. J. Cho, J. Seo, A lubricated nonimmunogenic neural probe for acute insertion trauma minimization and long-term signal recording. *Adv. Sci.* 8, 2100231 (2021).
- 27. E. Mariani, G. Lisignoli, R. M. Borzì, L. Pulsatelli, Biomaterials: Foreign bodies or tuners for the immune response? *Int. J. Mol. Sci.* **20**, 636 (2019).
- B. Bruna, P. Lobos, R. Herrera-Molina, C. Hidalgo, A. Paula-Lima, T. Adasme, The signaling pathways underlying BDNF-induced Nrf2 hippocampal nuclear translocation involve ROS, RyR-Mediated Ca²⁺ signals, ERK and PI3K. *Biochem. Biophys. Res. Commun.* 505, 201–207 (2018).
- P.-H. Lin, B.-R. Li, Antifouling strategies in advanced electrochemical sensors and biosensors. *Analyst* 145, 1110–1120 (2020).
- J. Park, D. Jeong, Y. Lee, K. Park, T. Y. Kim, J. H. Choi, W. Y. Jang, J. Seo, Bioactivated lubricant-infused surfaces: A dual-action strategy for enhancing osseointegration and preventing implant-associated infections. Chem. Eng. J. 482, 149043 (2024).
- J. R. Eles, A. L. Vazquez, N. R. Snyder, C. Lagenaur, M. C. Murphy, T. D. Kozai, X. T. Cui, Neuroadhesive L1 coating attenuates acute microglial attachment to neural electrodes as revealed by live two-photon microscopy. *Biomaterials* 113, 279–292 (2017).
- N. Kushwah, K. Woeppel, V. Dhawan, D. Shi, X. T. Cui, Effects of neuronal cell adhesion molecule L1 and nanoparticle surface modification on microglia. *Acta Biomater.* 149, 273–286 (2022).
- A. Golabchi, K. M. Woeppel, X. Li, C. F. Lagenaur, X. T. Cui, Neuroadhesive protein coating improves the chronic performance of neuroelectronics in mouse brain. *Biosens. Bioelectron.* 155, 112096 (2020).
- S. Russell, H. Eley, M. Tisdale, Role of reactive oxygen species in protein degradation in murine myotubes induced by proteolysis-inducing factor and angiotensin II. *Cell. Signal.* 19, 1797–1806 (2007).
- C. Hu, D. Ashok, D. R. Nisbet, V. Gautam, Bioinspired surface modification of orthopedic implants for bone tissue engineering. *Biomaterials* 219, 119366 (2019).
- M. Badv, J. I. Weitz, T. F. Didar, Lubricant-infused PET grafts with built-in biofunctional nanoprobes attenuate thrombin generation and promote targeted binding of cells. Small 15, 1905562 (2019).
- J. Saba, J. Turati, D. Ramirez, L. Carniglia, D. Durand, M. Lasaga, C. Caruso, Astrocyte truncated-TrkB mediates BDNF antiapoptotic effect leading to neuroprotection. J. Neurochem. 146. 686–702 (2018).
- J. R. Liddell, S. Lehtonen, C. Duncan, V. Keksa-Goldsteine, A.-L. Levonen, G. Goldsteins, T. Malm, A. R. White, J. Koistinaho, K. M. Kanninen, Pyrrolidine dithiocarbamate activates the Nrf2 pathway in astrocytes. J. Neuroinflammation 13, 49 (2016).
- N. Schmidt, J. Schulze, D. P. Warwas, N. Ehlert, T. Lenarz, A. Warnecke, P. Behrens, Long-term delivery of brain-derived neurotrophic factor (BDNF) from nanoporous silica nanoparticles improves the survival of spiral ganglion neurons in vitro. PLOS ONE 13, e0194778 (2018).
- Z. Ding, L. Song, Q. Wang, G. Kumar, Y. Yan, C. Ma. Astrocytes: A double-edged sword in neurodegenerative diseases. *Neural Regen. Res.* 16, 1702–1710 (2021).
- J. Saba, J. Turati, D. Ramírez, L. Carniglia, D. Durand, M. Lasaga, C. Caruso, Astrocyte truncated tropomyosin receptor kinase B mediates brain-derived neurotrophic factor anti-apoptotic effect leading to neuroprotection. J. Neurochem. 146, 686–702 (2018).
- S. Bathina, U. N. Das, Brain-derived neurotrophic factor and its clinical implications. Arch. Med. Sci. 11, 1164–1178 (2015).
- 43. C. E. McGregor, A. W. English, The role of BDNF in peripheral nerve regeneration: Activity-dependent treatments and Val66Met. Front. Cell. Neurosci. 12, 522 (2019).
- M. Swain, S. K. Soman, K. Tapia, R. Y. Dagda, R. K. Dagda, Brain-derived neurotrophic factor protects neurons by stimulating mitochondrial function through protein kinase A. J. Neurochem. 167, 104–125 (2023).
- Y. Hu, H. Zou, Z. Zhong, Q. Li, Q. Zeng, Q. Ouyang, X. Zou, M. Wang, Y. Luo, D. Yao, The role of astrocyte-neuron lactate shuttle in neuropathic orofacial pain. *J. Oral Rehabil.* 51, 2513–2528 (2024).
- R. L. Akkermans, N. A. Spenley, S. H. Robertson, COMPASS III: Automated fitting workflows and extension to ionic liquids. *Mol. Simul.* 47, 540–551 (2021).
- H. J. C. Berendsen, J. P. M. Postma, W. F. Van Gunsteren, A. DiNola, J. R. Haak, Molecular dynamics with coupling to an external bath. J. Chem. Phys. 81, 3684–3690 (1984).
- B. Delley, An all-electron numerical method for solving the local density functional for polyatomic molecules. J. Chem. Phys. 92, 508–517 (1990).
- J. P. Perdew, K. Burke, M. Ernzerhof, Generalized gradient approximation made simple. Phys. Rev. Lett. 77, 3865–3868 (1996).

SCIENCE ADVANCES | RESEARCH ARTICLE

- A. Tkatchenko, M. Scheffler, Accurate molecular van der Waals interactions from ground-state electron density and free-atom reference data. Phys. Rev. Lett. 102, 073005 (2009).
- S. A. Liddelow, K. A. Guttenplan, L. E. Clarke, F. C. Bennett, C. J. Bohlen, L. Schirmer, M. L. Bennett, A. E. Münch, W. S. Chung, T. C. Peterson, D. K. Wilton, A. Frouin, B. A. Napier, N. Panicker, M. Kumar, M. S. Buckwalter, D. H. Rowitch, V. L. Dawson, T. M. Dawson, B. Stevens, B. A. Barres, Neurotoxic reactive astrocytes are induced by activated microglia. Nature 541, 481–487 (2017).
- 52. Y. Hwang, H.-C. Kim, E.-J. Shin, Effect of rottlerin on astrocyte phenotype polarization after trimethyltin insult in the dentate gyrus of mice. *J. Neuroinflammation* **19**, 142 (2022).
- A. Tassoni, V. Farkhondeh, Y. Itoh, N. Itoh, M. V. Sofroniew, R. R. Voskuhl, The astrocyte transcriptome in EAE optic neuritis shows complement activation and reveals a sex difference in astrocytic C3 expression. *Sci. Rep.* 9, 10010 (2019).
- 54. A. King, B. Szekely, E. Calapkulu, H. Ali, F. Rios, S. Jones, C. Troakes, The increased densities, but different distributions, of both C3 and S100A10 immunopositive astrocyte-like cells in Alzheimer's disease brains suggest possible roles for both A1 and A2 astrocytes in the disease pathogenesis. *Brain Sci.* 10, 503 (2020).

Acknowledgments

Funding: This work was supported by the National Research Foundation of Korea grant RS-2025-02214081 (to J.S.), National Research Foundation of Korea grant RS-2025-02219306 (to J.S.), National Research Foundation of Korea grant RS-2023-00207970 (to S.P.), and Boston-Korea Project RS-2024-00467213 (to S.P.). Author contributions: Conceptualization: T.Y.K., Y.S., J.S., and S.P. Methodology: T.Y.K., Y.S., J.S., and S.P. Investigation: T.Y.K., Y.S., K.-Y.K., D.G.L., Y.K., S.J.K., K.P., Y.L., T.K.L., J.J.C., and C.Y. Visualization: T.Y.K. and Y.S. Supervision: J.S. and S.P. Writing—original draft: T.Y.K., Y.S., J.S., and S.P. Writing—review and editing: T.Y.K., Y.S., J.S., and S.P. Competing interests: The authors declare that they have no competing interests.

Data and materials availability: All data needed to evaluate the conclusions in the paper are present in the paper and/or the Supplementary Materials.

Submitted 19 May 2025 Accepted 11 August 2025 Published 10 September 2025 10.1126/sciadv.adz1228